RSC Advances

PAPER

View Article Online
View Journal | View Issue

Cite this: *RSC Adv.*, 2020, **10**, 37956

Controlling the wettability of stainless steel from highly-hydrophilic to super-hydrophobic by femtosecond laser-induced ripples and nanospikes

Andrius Žemaitis,[a]* Alexandros Mimidis,[b] Antonis Papadopoulos,[b] Paulius Gečys,[a] Gediminas Račiukaitis,[a] Emmanuel Stratakis[b] and Mindaugas Gedvilas[a]

Received 29th June 2020
Accepted 6th October 2020

DOI: 10.1039/d0ra05665k

rsc.li/rsc-advances

Results on the manipulation of the wetting properties of stainless steel alloy surface by ultrashort pulse laser texturing are presented. The wide range of water droplet contact angles from highly-hydrophilic to super-hydrophobic was achieved by generation of laser-induced periodic surface structures (LIPSS) and nanospikes. In particular, the wetting state was controlled by accumulated laser fluence, which determines the carbon/oxygen content and nano-texture type of the surface after laser treatment. A super-hydrophobic water-repelling surface was generated. The simple, single-step laser processing technology was demonstrated as a promising tool for the large-scale industrial production of self-cleaning stainless steel.

1. Introduction

Various complex surfaces on plants and animals found in nature evolved to maintain a specific function, which is responsible for the species survival. For example, super-hydrophobic lotus leaves with the self-cleaning ability,[1] desert beetles with combined super-hydrophobic and hydrophilic areas for fog harvesting and water transport[2,3] glasswing butterflies *Greta oto* with transparent, anti-reflective wings[4] and many more.[5–8] The artificial fabrication of functional surfaces is not a simply accomplishable task. The dual-scale hierarchical structures with resolution ranging from nano to micro are needed to successfully mimic a particular surface with optical,[9–11] wetting[12,13] or tribological[14,15] properties. Due to the confined laser–matter interaction area, the ultrashort laser pulses gives a possibility to reach a precise structuring in the scale of micrometres by direct laser writing technique *via* ablation. Surface structuring by ultrashort pulses is possible even below the light diffraction limit due to generation of self-organised structures like laser-induced periodic surface structures (LIPSS)[11,16–18] and nanoparticles.[10,19]

The usage of stainless steel surfaces with altered wetting properties is wide and could be applied for many applications. It was already shown that stainless steel covered by LIPSS results in hydrophobicity and reduces bacterial adhesion, therefore creates antibacterial materials, which is used in medical device and food handling industries.[20,21] Also, in addition to the anti-bacterial properties super-hydrophobic nanoparticles deposited on stainless steel substrate exhibited enhanced corrosion resistance.[22] Super-hydrophobic stainless steel meshes were used for oil/water separation and self-cleaning applications.[23] The resistance to corrosion, contamination and bacteria are all well desired properties, which can be achieved by laser micro-/nanostructuring and control of the wettability.

The laser-based processes for stainless steel surface wettability control were investigated by ablation of trenches and generation of LIPSS.[13,24] The laser processing parameters, as interline separation for grid patterning and polarisation for LIPSS generation, are proven to be key factors for the fabrication of super-hydrophobic surfaces. The static contact angle coverage for steel *via* laser structuring is between ~90°–150°.[13,24–26] Ultrashort laser structuring provides the significant advantages *versus* the other techniques like radiofrequency plasma treatment[27] or additional surface layer coating[28] as it does not require the multiple-steps, vacuum environment or additional chemical consumables. However, to the best of our knowledge, there is no research work found in scientific literature exploring a single-step technique with the ability of tuning wetting state of stainless steel from highly-hydrophilic to super-hydrophobic.

In this research, we are presenting a simple, single-step procedure for stainless steel wetting control *via* femtosecond laser structuring. The wetting properties of the textured surfaces were altered from initial highly-hydrophilic to super-hydrophobic by varying the laser irradiation dose. The static contact angle (CA) of a water droplet on irradiated steel surface was varied from 4° to the super-hydrophobic state, where it was

[a]*Department of Laser Technologies (LTS), Center for Physical Sciences and Technology (FTMC), Savanoriu Ave. 231, 02300 Vilnius, Lithuania. E-mail: andrius.zemaitis@ftmc.lt*

[b]*Institute of Electronic Structure and Laser (IESL), Foundation for Research and Technology (FORTH), N. Plastira 100, Vassilika Vouton, 70013 Heraklion, Crete, Greece*

impossible to stick the droplet on the surface with the water bouncing from the laser-textured area. Initial stainless steel surface consisted of grains with dimensions of tens of micrometres. The grains were responsible for the hydrophilicity and Wenzel wetting state of the rough surface,[29] due to complete water filling of the grooves of the grain boundaries. The change of wetting properties started together with the formation of ripples on the grainy surface of stainless steel. The boundaries between the grains were gradually vanished due to over domination of LIPSS with increased laser fluence. Ripples in nanoscale were responsible for hydrophobicity and Cassie–Baxter state of the rough surface,[30] where water rests on top of the ripples with air trapped beneath. In addition to surface structure, a chemical elemental analysis was performed, and the role of surface chemistry for wetting state was discussed.

2. Materials and methods

2.1 Laser structuring

An ytterbium-doped potassium gadolinium tungstate (Yb:KGW) laser (Pharos, Light Conversion) was used to produce linearly polarised pulses of $\tau = 170$ fs duration, $f = 100$ kHz repetition rate, and $\lambda = 1026$ nm central wavelength. A maximum average optical power on the sample surface was $P = 3.3$ W. A galvanometer scanner and F-theta lens with a focal distance of 290 mm were used to scan and focus the laser beam. Focused beam diameter on the sample surface was $2w_0 = 100$ μm ($1/e^2$ level) and kept constant during experiments. Rectangular areas of 11 × 11 mm^2 were laser irradiated while the processing parameters were varied. For the first experiment, horizontal lines separated by a fixed hatch distance of $\Delta h = 5$ μm were scanned at $v = 1$ m s^{-1} speed and average laser power was varied from 0.1 W to 3.3 W (15 tests). For the second experiment, the laser power of $P = 3.3$ W and scanning speed of $v = 50$ mm s^{-1} were used while the hatch distance Δh was changed from 10 μm to 110 μm (11 tests). Also, the grid scanning strategy was used, which consisted of vertical and horizontal lines with Δh separation. The accumulated fluence was calculated by $F_{ACC} = 2P/v\Delta h$.

2.2 LIPSS periodicity

Scanning electron microscope (SEM) images were used to calculate the spatial period Λ of LIPSS. Two-dimensional (2D) Fast Fourier Transformations (FFT) of SEM images were performed by open-source software (Gwyddion, Version 2.55). The periodicity Λ of LIPSS was extracted from 2D-FFT profiles by measuring the distance between two mirror-like related peaks both fitted by the Lorentz function: $\Lambda = 2/f_1 - f_2$, where f_1 and f_2 are the spatial frequencies in the 2D-FFT profile (Fig. 1). The error $\Delta\Lambda$ of the spatial period Λ was calculated from the full width at half maximum (FWHM) of the Lorentz fit. In most cases, four characteristic peaks were observed, two of them related to low spatial frequency LIPSS (LSFL) and two to high spatial frequency LIPSS (HSFL). Ripples are called HSFL when the spatial period is smaller than a half of the laser wavelength $\Lambda < \lambda/2$.[17]

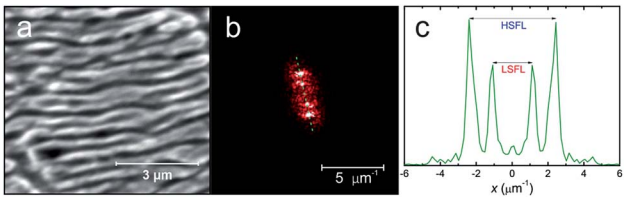

Fig. 1 Graphical representation of LIPSS periodicity measurement procedure: (a) SEM picture of LIPSS on stainless steel produced by the laser fluence of $F_0 = 0.44$ J cm^{-2}; (b) generated 2D-FFT image of SEM picture; (c) profile of the green dashed line from the 2D-FFT image with peaks representing spatial frequencies of HSFL and LSFL.

2.3 Wettability measurements

The CA characterisation was performed by using the optical contact angle measuring and contour analysis system (OCA 15EC, Data-Physics Instruments GmbH) equipped with a CCD camera to capture lateral images of water droplets applied on laser-structured and untreated steel. A droplet of deionised water with the volume of 3 μL was deposited by using a pipette (1–10 μJ Transferpette®, Brand). The camera, the water droplet and the illumination source equipped with a light-emitting diode were aligned into one line. Therefore, the droplet shadow was projected and captured by the digital camera. Average values of CA and measurement errors were obtained by a software (SCA20, Data-Physics Instruments GmbH). CA was considered to be 150° for the super-hydrophobic surfaces where the measurement was not performed as it was impossible to stick the droplet on top of the sample. All CA measurements were done 15 days after the laser structuring, therefore, preventing the instabilities of CA change during the first 10 days after laser irradiation.[31] Surface free energy of textured stainless steel was calculated by Owens–Wendt method, where two liquids are used to measure the contact angles with solid surfaces, usually applied for polymers and metals.[32] The polar liquid was distilled water (surface free energy $\gamma_w = 72.8$ mJ m^{-2}, dispersive component $\gamma_w^d = 21.8$ mJ m^{-2} and polar component $\gamma_w^p = 51.0$ mJ m^{-2})[33] the dispersive liquid was hexadecane ($C_{16}H_{34}$) (surface free energy $\gamma_w = 27.6$ mJ m^{-2}, dispersive component $\gamma_h^d = 27.6$ mJ m^{-2} and polar component $\gamma_h^p = 0$ mJ m^{-2}).[34,35]

2.4 Sample characterisation

The bulk stainless steel (1.4301) samples with dimensions of 50 × 50 × 5 mm^3 and surface roughness of $R_a < 0.3$ μm were used as a target material for laser structuring. For the sample visualisation and chemical element analysis, SEM (JSM-6490LV, JEOL) equipped with the X-ray energy dispersive spectroscopy (EDS) (X-Max, Oxford Instruments) were used. The elemental analysis was carried out with the 20 kV accelerating voltage and 50 nm electron beam spot size, limiting spatial resolution of the EDS spectrometer to 10 μm. The atomic chemical composition of the stainless steel at laser-untreated area measured by the EDS spectrometer was 35.9 at% C, 8.2 at% O, 11.0 at% Cr, 0.8 at% Mn, 39.8 at% Fe, 4.3 at% Ni. A stylus profiler (Dektak 150, Veeco) was used to measure the surface roughness R_a of an

untreated samples with micro-scale grains. Atomic force microscope (AFM) (Dimension Edge, Bruker) was utilised for measurements of nano-scale laser-induced ripples. Height distribution measurements of 10 × 10 μm^2 surface areas were performed in tapping mode and ambient conditions. A commercial silicon probe with a tip diameter of <10 nm (force constant – 40 N m^{-1}) was used.

3. Results and discussion

3.1 Formation of ripples

Ripples on stainless steel surface were produced by a raster scanning the femtosecond laser beam at high speed of v = 1 m s^{-1} and hatch distance of Δh = 5 μm resulting in the fabrication rate of 5 mm^2 s^{-1}. The average power P was varied from 0.1 W to 3.3 W, corresponding to the peak laser fluence F_0 range from 0.03 J cm^{-2} to 0.84 J cm^{-2}, calculated by $F_0 = P/\pi w_0^2 f$. The average number of pulses per spot area was $N = 157$ in this processing case. The formation of LIPSS on the steel started at a laser fluence of F_0 = 0.08 J cm^{-2} with low areal density and the spatial period around $\Lambda_{\mathrm{LSFL}} = 0.7 \pm 0.4$ μm (Fig. 2). The high spatial period error was the consequence of irregular LIPSS distribution. Steel irradiated by laser fluences lower than F_0 = 0.08 J cm^{-2} was visually the same as untreated one. The boundaries between grains were clearly visible with a grain size from ~5 μm to ~20 μm. After the laser fluence was further increased, the error of the spatial period stabilised down to a minimum value of $\Delta\Lambda$ = 0.1 μm due to more regular ripples. With a low laser fluence, LIPSS were formed on top of the grains. With increasing the fluence, the boundaries have gradually vanished, and at the fluence of F_0 = 0.25 J cm^{-2}, the grain boundaries were entirely hidden by ripples. The average periodicity of LIPSS was around Λ_{LSFL} = 0.75 μm for the fluence interval $F_0 = [0.08; 0.84]$ J cm^{-2}. This kind of ripples, where $\Lambda > \lambda/2$, is called low spatial frequency LIPSS (LSFL). Together with LSFL at certain fluences, high spatial frequency LIPSS (HSFL) were observed as well, which are also called nanoripples. The spatial period of HSFL was approximately half of LSFL size with the periodicity of $\Lambda_{\mathrm{HSFL}} \simeq 0.45$ μm. The HSFL appeared together with LSFL as dividing one ripple into two nanoripples. In order to apply a higher number of pulses per spot, the beam scanning speed was lowered to v = 50 mm s^{-1}. The laser fluence was kept at F_0 = 0.84 J cm^{-2} and hatch distance was varied from 10 μm to 110 μm, corresponding to pulses per spot from 3141 to 285, respectively. For the lowest hatch distance, an intense material ablation and the formation of nanospikes on the irradiated area were obtained instead of ripples.

When the hatch distance was increased, the formation of ripples started to appear (Fig. 3). For the hatch distance of 30 μm, the periodical surface structures were covered by nanospikes, while for 40 μm, the ripples were dominant, and only a hint of nanospikes was visible. When the hatch distance exceeded 90 μm, individual scan lines were distinguishable.

3.2 Wettability

The untreated steel surface was hydrophilic and had a CA of 4°. The grains, present on the stainless steel surface, induced the roughness which was responsible for the Wenzel wetting state and the hydrophilicity.[29] In this wetting state water filled the grooves of the grain boundaries. The depth of these grooves was in the range of ~1–2 μm resulting in R_a = 0.3 μm. The similar CA was measured for the laser-irradiated surfaces by laser fluence smaller than the LIPSS generation threshold. While the peak fluence was increased, the transition from the hydrophilic to the hydrophobic surface was observed (Fig. 4). The increase of contact angle correlated well with the laser-induced ripples formation, which smoothly covered the grains present at the native surface forming the Cassie–Baxter wetting state.[30] In this state, water rests on ripples with air trapped beneath. The typical depth of ripples was about ~0.1–0.4 μm with surface roughness of R_a = 0.2 μm measured by AFM. The creation of ripples on nano-scale and smoothing the grooves in micro-scale resulted in increased surface repellence to water. In the case of rapid 5 mm^2 s^{-1} (scanning speed v = 1 m s^{-1} and hatch distance Δh = 5 μm) processing, the highest CA was 135°. In order to obtain super-hydrophobic surface, the beam scanning

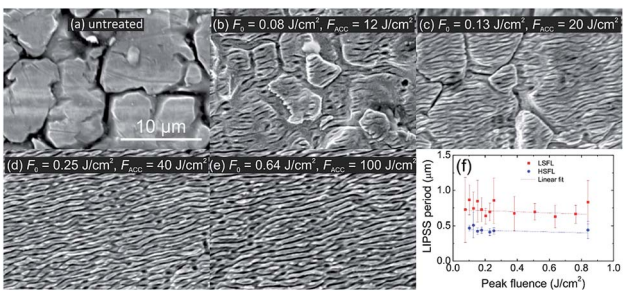

Fig. 2 Evolution of laser-induced ripple formation with increased peak fluence. (a–e) The grainy surface of stainless steel is being covered by LIPSS until the boundaries of grains have vanished. Scale bar in (a) is for all SEM images. (f) Periodicity of LIPSS measured by 2D-FFT of SEM images shows two main periods of LSFL at Λ_{LSFL} = 0.75 μm and HSFL at Λ_{HSFL} = 0.45 μm. The pulse repetition rate f = 100 kHz, beam scanning speed v = 1 m s^{-1}, hatch distance Δh = 5 μm, pulse duration τ = 170 fs, laser wavelength λ = 1026 nm.

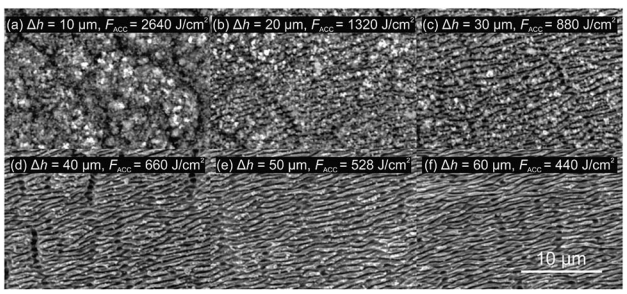

Fig. 3 SEM images of laser-induced nanospikes and ripples after laser irradiation with various hatch distance Δh ranging from 10 μm to 60 μm, step 10 μm. (a and b) The surface of stainless steel textured by nanospikes; (c) surface textured by ripples and nanospikes; (d–f) surface textured by ripples. Scale bar in (f) is for all SEM images. The laser fluence F_0 = 0.84 J cm^{-2}, pulse repetition rate f = 100 kHz, beam scanning speed v = 50 mm s^{-1}, pulse duration τ = 170 fs, laser wavelength λ = 1026 nm.

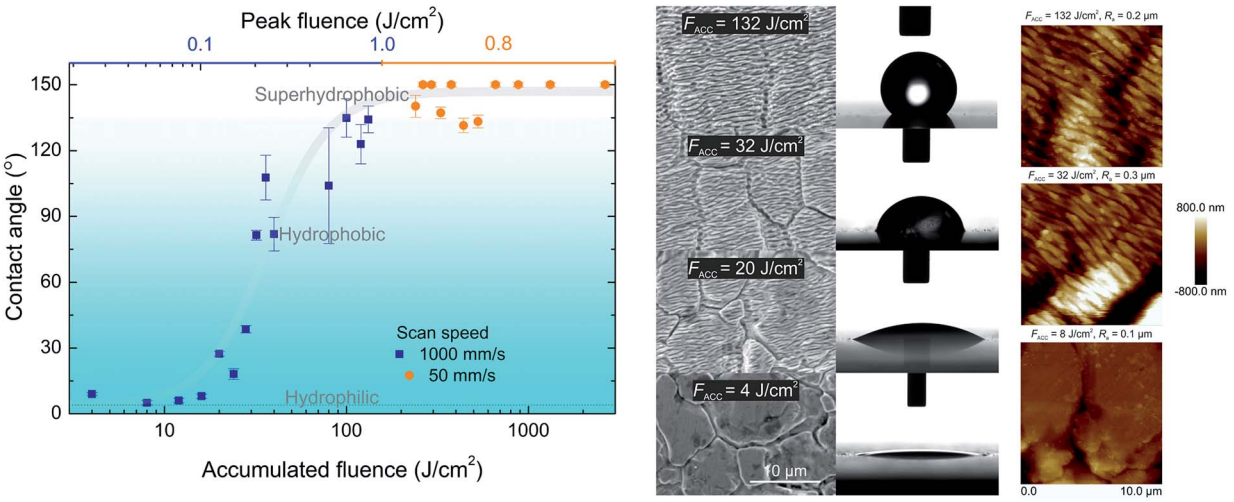

Fig. 4 Water droplet contact angle with laser-textured stainless steel surface *versus* the accumulated fluence. The blue squares present the contact angle measurement results when the pulse energy was varied, keeping the scanning speed $v = 1$ m s^{-1}, hatch distance $\Delta h = 5$ μm; orange circles – the hatch distance variation, with fixed scanning speed $v = 50$ mm s^{-1}, and peak fluence $F_0 = 0.84$ J cm^{-2}. On the right – SEM, CCD camera and AFM pictures showing the evolution of ripples formation with increased accumulated fluence and corresponding water droplet with ascending contact angle from bottom to top. Images of 3 μL water droplets on laser-textured steel surfaces show the transition from the highly-hydrophilic (bottom) to hydrophobic (top) surface. The pulse repetition rate $f = 100$ kHz, pulse duration $\tau = 170$ fs, laser wavelength $\lambda = 1026$ nm.

speed was reduced to $v = 50$ mm s^{-1} to generate a higher accumulated fluence on the sample surface. In this case, the accumulated fluence was varied by changing the hatch distance between the scanned lines. The lowest hatch distance corresponded to the highest accumulated fluence and *vice versa*. For example, at the hatch distance of $\Delta h = 10$ μm, the accumulated fluence was 2640 J cm^{-2} and for $\Delta h = 110$ μm to 240 J cm^{-2}. For the higher accumulated fluence, the super-hydrophobic surface was fabricated. It was impossible to measure the contact angle for the super-hydrophobic surfaces due to their high water repellent properties. For the cases where it was impossible to stick the droplet on the laser processed area, the contact angle was assumed to be 150°. The lowest accumulated fluence for which the super-hydrophobic state was observed was 264 J cm^{-2} (scanning speed $v = 50$ mm s^{-1} and hatch distance $\Delta h = 100$ μm). The full contact angle range, from the initial hydrophilic to super-hydrophobic surface, was fabricated by the femtosecond laser texturing. We can assume that the key parameter responsible for the surface wetting is the accumulated fluence.

Surface free energy of textured surfaces was calculated by equations derived for the square roots of dispersive $(\gamma_s^d)^{0.5}$ and polar $(\gamma_s^p)^{0.5}$ components.[32] The highly-hydrophilic stainless steel exhibited highest values of polar component $(\gamma_s^p)^{0.5} = 6.1$ (mJ m^{-2})$^{0.5}$ while dispersive component had values of $(\gamma_s^d)^{0.5} =$ 5.2–5.3 (mJ m^{-2})$^{0.5}$ for all surfaces from highly-hydrophilic to super-hydrophobic. The polar component $(\gamma_s^p)^{0.5}$ decreased gradually with the change of the surface structure and formation of ripples and nanospikes until the point, where super-hydrophobic surface had negative values of polar component $(\gamma_s^p)^{0.5} < 0$ (mJ m^{-2}).$^{0.5}$ The total surface free energy ($\gamma_s = \gamma_s^d + \gamma_s^p$) of stainless steel was $\gamma_s = 42.3$ mJ m^{-2} for super-hydrophobic nanospikes, $\gamma_s = 32.4$ mJ m^{-2} for hydrophobic ripples and $\gamma_s = 65.2$ mJ m^{-2} for highly-hydrophilic grains.

3.3 Chemical analysis

In addition to the surface structure, hydrophobic and hydrophilic properties of the material are strongly influenced by its chemical composition. Usually, the surface of metals and their alloys are covered by oxide films of those metals, resulting in high surface energy and hydrophilic properties. However, the situation changes when the surface is exposed to laser irradiation or other aggressive conditions that initiate adsorption, chemisorption and chemical interactions of gases or moisture presented in ambient air with the surface. It is well known that hydrophilic surfaces with the high surface energy are rich in polar functional groups (–CO, –OH, –NH_2, –COOH, …), while hydrophobic-non-polar (alkyl, fluoralkyl groups, –SH, …). All these statements suggest (assuming that the morphology of all surfaces is the same) that as the oxygen content increases, the surface hydrophilicity should increase as well while increasing carbon content (for example chemisorption of non-polar hydrocarbons presented in an air atmosphere) leads to hydrophobic properties. The corresponding dependence has been described in many scientific articles.[31,36,37] However, the EDS analysis of our experiments showed completely opposite results coinciding with other works.[38,39] The carbon content was highest for the laser fluence below the ripple formation threshold and dropped down about four times when the ripple generation started. The oxygen content was significantly increased at the high accumulated fluence values. Such behaviour could be explained by decomposition of CO_2 (present in ambient air) following by the reaction with a non-stoichiometric oxygen-deficient active magnetite $Fe_3O_{4-\delta}$ ($0 < \delta < 1$) created during the laser irradiation process.[31] The decomposition reaction of one CO_2 molecule generates one C atom settling on the surface of the alloy, and two O^{2-} ions which are transferring to oxygen vacancies in $Fe_3O_{4-\delta}$ resulting in the formation of

stoichiometric Fe_3O_4.[40] As a result, oxygen-to-carbon (O/C) atomic percentage ratio increases together with the increase of the accumulated laser fluence (Fig. 5 inset). Similar results of O/C ratio increase with an increase of the number of laser pulses per spot for stainless steel textured by LIPSS using femtosecond laser was reported by Razi *et al.*[41] In contradiction, almost constant O/C ratio with the increase of the irradiation dose has been observed in our previous work.[42] However, the irradiation dose has been varied just up to 30 J cm^{-2}. The contact angle dependence on the oxygen-to-carbon ratio is depicted in Fig. 5. The static CA of ~7° was observed for the O/C ratio smaller than 0.35. The steep rise of static CA from ~7° up to ~150° was observed for the O/C ratios from 0.35 to 0.45. The super-hydrophobic state with a non-changing static CA > 150° for the O/C ratios ranging from 0.45 to 2.2 was registered. The O/C ratio clearly is responsible for the wetting state change of stainless steel surface, treated by femtosecond pulses. Similar results of static CA rise from 136° to 173° with the increase of O/C percentage per weight ratio from 1.23 to 3.6 on stainless steel textured by LIPSS using a picosecond laser was observed by Faas *et al.*[39] It is essential to mention that both stoichiometric and non-stoichiometric magnetite are metal oxides and, independent of the presence or absence of oxygen vacancies, are polar. They both have high surface energy and exhibit strong hydrophilic properties. On the other hand, elemental carbon and carbon derivatives show hydrophobic properties.[43–45] Therefore, the attachment of two oxygen ions does not significantly affect the increase in hydrophilic properties. Contrary, the deposition of one carbon atom strongly induces the surface hydrophobicity and the percentage increase in oxygen leading to a percentage decrease in carbon as observed in EDS analysis. The real increase in both, carbon and oxygen elements amount, is confirmed by the decreasing of the other elements' joint percentage amount.

This phenomenon was also confirmed by the significant increase in oxygen content when nanospikes were formed (at the high accumulated fluence values of ~1 kJ cm^{-2}). The smaller the particle size was, the larger the oxygen-deficient degree was, resulting in the higher activity of the CO_2 decomposition.[40] Furthermore, materials made up of nanospikes have a relatively larger surface area when compared to the same volume of material made up of bigger particles, therefore the interaction area increases. Nevertheless, all these considerations are assumptions and a more thorough chemical analysis should be performed to explain the role of surface chemistry for the hydrophobicity.

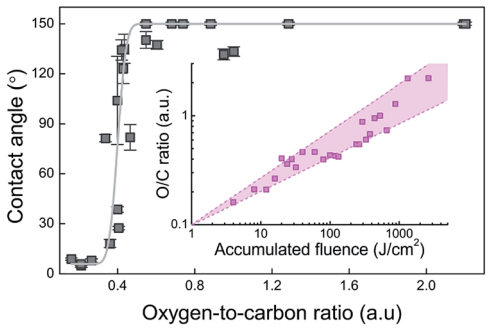

Fig. 5 Contact angle dependence on the oxygen-to-carbon (O/C) ratio in the laser-textured stainless steel. Inset: O/C ratio *versus* accumulated laser fluence. The pulse repetition rate $f = 100$ kHz, pulse duration $\tau = 170$ fs, laser wavelength $\lambda = 1026$ nm.

4. Conclusions

Femtosecond laser beam scanning was applied for stainless steel surface structuring. By varying the accumulated laser fluence from 4 J cm^{-2} to 2.6 kJ cm^{-2}, the wide range of water droplet contact angles ranging from 4° to 150° on the irradiated stainless steel surface was measured. The initial highly-hydrophilic surface was gradually changed into super-hydrophobic one by laser-induced ripples and at the high accumulated fluences – nanospikes. The wetting state transition started together with the generation of ripples proving that surface structuring by ripples was responsible for surface wetting. Also, we discussed the possible mechanism of surface chemistry change due to the decomposition of CO_2 molecules present in ambient air and followed by reaction with a non-stoichiometric oxygen-deficient active magnetite $Fe_3O_{4-\delta}$ ($0 < \delta < 1$) created in the laser irradiation process. The variation of stainless steel wetting state was altered by ultrafast laser processing and following change of surface chemistry. Nevertheless, we believe that the major role for the hydrophobic properties plays the femtosecond laser-induced surface structures.

Conflicts of interest

There are no conflicts to declare.

Acknowledgements

A. Ž. would like to thank the Research Council of Lithuania for funding the visit in Crete under grant agreements 09.3.3.-LMT-K-712-14-0137.

References

1 W. Barthlott and C. Neinhuis, *Planta*, 1997, **202**, 1–8.
2 W. J. Hamilton and M. K. Seely, *Nature*, 1976, **262**, 284–285.
3 A. R. Parker and C. R. Lawrence, *Nature*, 2001, **414**, 33–34.
4 R. H. Siddique, G. Gomard and H. Hölscher, *Nat. Commun.*, 2015, **6**, 6909.
5 B. Bhushan and Y. C. Jung, *Prog. Mater. Sci.*, 2011, **56**, 1–108.
6 F. A. Müller, C. Kunz and S. Gräf, *Materials*, 2016, **9**, 476.
7 B. Bhushan, *Philos. Trans. R. Soc., A*, 2009, **367**, 1445–1486.
8 D. P. Linklater, S. Juodkazis and E. P. Ivanova, *Nanoscale*, 2017, **9**, 16564–16585.
9 B. Dusser, Z. Sagan, H. Soder, N. Faure, J. P. Colombier, M. Jourlin and E. Audouard, *Opt. Express*, 2010, **18**, 2913–2924.

10 J.-M. Guay, A. C. Lesina, G. Cote, M. Charron, D. Poitras, L. Ramunno, P. Berini and A. Weck, *Nat. Commun.*, 2017, **8**, 16095.
11 A. Papadopoulos, E. Skoulas, A. Mimidis, G. Perrakis, G. Kenanakis, G. D. Tsibidis and E. Stratakis, *Adv. Mater.*, 2019, **31**, 1901123.
12 V. Zorba, E. Stratakis, M. Barberoglou, E. Spanakis, P. Tzanetakis, S. H. Anastasiadis and C. Fotakis, *Adv. Mater.*, 2008, **20**, 4049–4054.
13 C. Florian, E. Skoulas, D. Puerto, A. Mimidis, E. Stratakis, J. Solis and J. Siegel, *ACS Appl. Mater. Interfaces*, 2018, **10**, 36564–36571.
14 J. Bonse, R. Koter, M. Hartelt, D. Spaltmann, S. Pentzien, S. Höhm, A. Rosenfeld and J. Krüger, *Appl. Surf. Sci.*, 2015, **336**, 21–27.
15 A. Žemaitis, J. Mikšys, M. Gaidys, P. Gečys and M. Gedvilas, *Mater. Res. Express*, 2019, **6**, 065309.
16 G. D. Tsibidis, C. Fotakis and E. Stratakis, *Phys. Rev. B: Condens. Matter Mater. Phys.*, 2015, **92**, 041405.
17 J. Bonse, S. Höhm, S. V. Kirner, A. Rosenfeld and J. Krüger, *IEEE J. Sel. Top. Quantum Electron.*, 2017, **23**, 1.
18 A. Dostovalov, K. Bronnikov, V. Korolkov, S. Babin, E. Mitsai, A. Mironenko, M. Tutov, D. Zhang, K. Sugioka, J. Maksimovic, T. Katkus, S. Juodkazis, A. Zhizhchenko and A. Kuchmizhak, *Nanoscale*, 2020, **12**, 13431–13441.
19 C.-Y. Shih, I. Gnilitskyi, M. V. Shugaev, E. Skoulas, E. Stratakis and L. V. Zhigilei, *Nanoscale*, 2020, **12**, 7674–7687.
20 X. Zhang, L. Wang and E. Levänen, *RSC Adv.*, 2013, **3**, 12003–12020.
21 A. H. A. Lutey, L. Gemini, L. Romoli, G. Lazzini, F. Fuso, M. Faucon and R. Kling, *Sci. Rep.*, 2018, **8**, 10112.
22 H. Qian, M. Li, Z. Li, Y. Lou, L. Huang, D. Zhang, D. Xu, C. Du, L. Lu and J. Gao, *Mater. Sci. Eng., C*, 2017, **80**, 566–577.
23 Z. Zhang, H. Wang, Y. Liang, X. Li, L. Ren, Z. Cui and C. Luo, *Sci. Rep.*, 2018, **8**, 3869.
24 M. Martínez-Calderon, A. Rodríguez, A. Dias-Ponte, M. C. Morant-Miñana, M. Gómez-Aranzadi and S. M. Olaizola, *Appl. Surf. Sci.*, 2016, **374**, 81–89.
25 S. V. Kirner, U. Hermens, A. Mimidis, E. Skoulas, C. Florian, F. Hischen, C. Plamadeala, W. Baumgartner, K. Winands, H. Mescheder, J. Krüger, J. Solis, J. Siegel, E. Stratakis and J. Bonse, *Appl. Phys. A*, 2017, **123**, 754.
26 U. Hermens, S. V. Kirner, C. Emonts, P. Comanns, E. Skoulas, A. Mimidis, H. Mescheder, K. Winands, J. Krüger, E. Stratakis and J. Bonse, *Appl. Surf. Sci.*, 2017, **418**, 499–507.
27 T. Sönmez, M. Fazeli Jadidi, K. Kazmanli, Ö. Birer and M. Ürgen, *Vacuum*, 2016, **129**, 63–73.
28 A. Fihri, E. Bovero, A. Al-Shahrani, A. Al-Ghamdi and G. Alabedi, *Colloids Surf., A*, 2017, **520**, 378–390.
29 R. N. Wenzel, *Ind. Eng. Chem.*, 1936, **28**, 988–994.
30 A. B. D. Cassie and S. Baxter, *Trans. Faraday Soc.*, 1944, **40**, 546–551.
31 A.-M. Kietzig, S. G. Hatzikiriakos and P. Englezos, *Langmuir*, 2009, **25**, 4821–4827.
32 A. Rudawska, in *9 - Assessment of surface preparation for the bonding/adhesive technology: Surface Treatment in Bonding Technology*, ed. A. Rudawska, Academic Press, 2019, pp. 227–275.
33 C. J. Van Oss, L. Ju, M. K. Chaudhury and R. J. Good, *J. Colloid Interface Sci.*, 1989, **128**, 313–319.
34 B. Biliński, *Mater. Chem. Phys.*, 1987, **18**, 231–244.
35 M. Kobayashi, Y. Terayama, H. Yamaguchi, M. Terada, D. Murakami, K. Ishihara and A. Takahara, *Langmuir*, 2012, **28**, 7212–7222.
36 J. T. Cardoso, A. Garcia-Girón, J. M. Romano, D. Huerta-Murillo, R. Jagdheesh, M. Walker, S. S. Dimov and J. L. Ocaña, *RSC Adv.*, 2017, **7**, 39617–39627.
37 Z. Yang, X. Liu and Y. Tian, *J. Colloid Interface Sci.*, 2019, **533**, 268–277.
38 P. Bizi-bandoki, S. Valette, E. Audouard and S. Benayoun, *Appl. Surf. Sci.*, 2013, **273**, 399–407.
39 S. Faas, U. Bielke, R. Weber and T. Graf, *Sci. Rep.*, 2019, **9**, 1933.
40 C. Zhang, S. Li, L. Wang, T. Wu and S. Peng, *Mater. Chem. Phys.*, 2000, **62**, 44–51.
41 S. Razi and F. Ghasemi, *Eur. Phys. J. Plus*, 2018, **133**, 49.
42 P. Gečys, A. Vinčiunas, M. Gedvilas, A. Kasparaitis, R. Lazdinas and G. Račiukaitis, *J. Laser Micro/Nanoeng.*, 2015, **10**, 129–133.
43 K. K. S. Lau, J. Bico, K. B. K. Teo, M. Chhowalla, G. A. J. Amaratunga, W. I. Milne, G. H. McKinley and K. K. Gleason, *Nano Lett.*, 2003, **3**, 1701–1705.
44 M. Gonçalves, M. Molina-Sabio and F. Rodriguez-Reinoso, *J. Anal. Appl. Pyrolysis*, 2010, **89**, 17–21.
45 H. Yang, Y. Liu, Z. Guo, B. Lei, J. Zhuang, X. Zhang, Z. Liu and C. Hu, *Nat. Commun.*, 2019, **10**, 1789.